

The Entropic Signature of Class Speciation in Diffusion Models

Florian Handke ^{*1} Dejan Stančević ^{*2} Felix Koulischer ¹ Thomas Demeester ¹ Luca Ambrogioni ²

Abstract

Diffusion models do not recover semantic structure uniformly over time. Instead, samples transition from semantic ambiguity to class commitment within a narrow regime. Recent theoretical work attributes this transition to dynamical instabilities along class-separating directions, but practical methods to detect and exploit these windows in trained models are still limited. We show that tracking the class-conditional entropy of a latent semantic variable given the noisy state provides a reliable signature of these transition regimes. By restricting the entropy to semantic partitions, the entropy can furthermore resolve semantic decisions at different levels of abstraction. We analyze this behavior in high-dimensional Gaussian mixture models and show that the entropy rate concentrates on the same logarithmic time scale as the speciation symmetry-breaking instability previously identified in variance-preserving diffusion. We validate our method on EDM2-XS and Stable Diffusion 1.5, where class-conditional entropy consistently isolates the noise regimes critical for semantic structure formation. Finally, we use our framework to quantify how guidance redistributes semantic information over time. Together, these results connect information-theoretic and statistical physics perspectives on diffusion and provide a principled basis for time-localized control.

1. Introduction

Diffusion models have become state-of-the-art generative frameworks for images, audio, video, and multimodal settings (Sohl-Dickstein et al., 2015; Ho et al., 2020; Song et al., 2021b; Kong et al., 2021; Singer et al., 2023). In modern applications, their practical utility is closely linked

¹Department of Information Technology, Ghent University - imec, Ghent, Belgium ²Donders Institute for Brain, Cognition and Behaviour, Radboud University, Nijmegen, the Netherlands. Correspondence to: Florian Handke <florian.handke@ugent.be>, Dejan Stančević <dejan.stancevic@ru.nl>.

Preprint. February 11, 2026.

to their ability to follow conditioning signals (labels, text, or other modalities) by guiding the reverse-time denoising dynamics toward user-specified semantics (Dhariwal & Nichol, 2021; Ho & Salimans, 2022). Guidance, especially classifier-free guidance, underlies many of the most capable conditional generators, including GLIDE, Imagen, and DALL-E-style systems, as well as latent-diffusion-based models such as Stable Diffusion (Nichol et al., 2022; Shaha et al., 2022; Ramesh et al., 2022; Betker et al., 2023; Rombach et al., 2022). Despite the strong empirical performance of guided diffusion, the mechanisms by which semantic structure emerges during the denoising process, and how this emergence relates to actionable control in sampling, remain only partially understood.

A growing body of theoretical literature connects sampling in diffusion models with ideas from statistical physics, including dynamical instabilities, phase transitions, and symmetry breaking in high-dimensional stochastic flows (Biroli & Mézard, 2023; Biroli et al., 2024; Montanari, 2023; Montanari & Wu, 2023; Ambrogioni, 2025a). A prominent line of work studies the reverse-time dynamics under exact or near-exact score assumptions and identifies a sharp transition from semantic ambiguity to class commitment, termed symmetry-breaking class speciation (Raya & Ambrogioni, 2023; Biroli et al., 2024). In this picture, speciation corresponds to a time when the coarse structure of the data is revealed similar to spontaneous symmetry breaking in statistical physics. Complementary studies show that guidance interacts non-trivially with these dynamical regimes particularly in high dimensions, helping to explain why classifier-free guidance is effective in practice despite known low-dimensional pathologies (Pavasovic et al., 2025). In parallel, empirical and theoretical results report the emergence of phase-transition-like features and narrow critical windows along the sampling trajectory, suggesting that different semantic attributes are determined at different noise scales (Sclocchi et al., 2025; Li & Chen, 2024). However, existing theories do not provide an operational quantity that tracks semantic commitment along the sampling trajectory, aligns with the symmetry-breaking/speciation picture, and can be directly estimated in trained diffusion models.

(i) We show that class-conditional entropy provides such an operational marker of speciation in high-dimensional Gaussian mixtures; (ii) we demonstrate that this signal can be

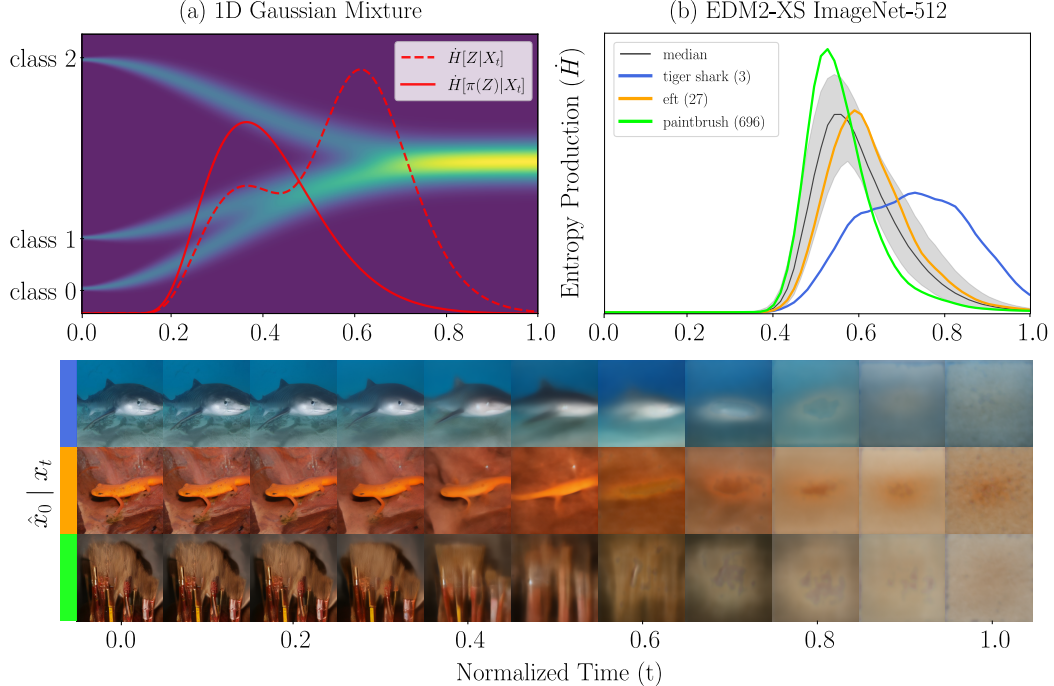


Figure 1. Overview of entropy production in generative diffusion. (a) Entropy production quantified as the temporal derivative of the conditional entropy during the denoising process. The dashed curve shows the class-conditional entropy production over the full label space, capturing semantic commitment at the level of the complete class variable. The solid curve shows the partitioned class-conditional entropy production for the binary decision between class 0 and class 1, isolating when this specific semantic distinction is resolved. (b) Entropy production in a real dataset. Each curve shows the partitioned class-conditional entropy production for a single class against its complement. The lower panel displays representative noiseless predictions along the denoising trajectory for the highlighted classes, illustrating how semantic structure emerges around the corresponding entropy production peaks.

estimated in trained diffusion models and allows isolating emergence of specific semantic elements in practice; and (iii) we use it to analyze how guidance redistributes semantic information over time. Figure 1 illustrates the entropy production, i.e., the temporal derivative of the class conditional entropy, in both a simple one-dimensional setting and a realistic dataset.

We validate our theory on synthetic Gaussian mixtures and demonstrate its practical relevance on EDM2 (Karras et al., 2024) and Stable Diffusion (Rombach et al., 2022), trained on ImageNet (Deng et al., 2009) and LAION5B (Schuhmann et al., 2022), respectively. In all settings, class-conditional entropy consistently identifies the noise regimes in which class-specific features emerge and quantifies the distortion of information recovery induced by guidance, thus complementing recent empirical findings on its limited effectiveness in low and high noise regimes (Kynkäanniemi et al., 2024; Koulischer et al., 2025b).

2. Related Work

Information theory In recent years, the connection between diffusion models and information theory has been studied in more detail. Kong et al. (2023) explore the

information-theoretic underpinnings of diffusion models and provide practical estimators for likelihood-related quantities, while Franzese et al. (2024) show how score-based diffusion models can be used to estimate mutual information (and related entropic quantities). Premkumar (2025) studies properties of a trajectory-level entropy motivated by stochastic-thermodynamic viewpoints. In his later work, Premkumar (2026) draws an analogy between diffusion models and Kelly criteria, giving a direct relation to the amount of additional information required to store class-conditional structure. Stancevic et al. (2025), on the other hand, focus on using an entropy-based scheduler to accelerate sampling in such a way that each step contributes a comparable information gain to the final sample. Ambrogi (2025b) further develops this viewpoint and connects it to the physics picture of diffusion, establishing entropy and information flow as central quantities for analyzing diffusion dynamics.

While Wang et al. (2025) use mutual information between the text prompt and the final generated image as an explicit alignment objective and diagnostic for prompt-conditioned generation, Kong et al. (2024) treat mutual information and related information-decomposition quantities as interpretability signals that attribute how different factors con-

tribute to the final sample. In both cases, mutual information summarizes how strongly the conditioning affects the output. By contrast, we treat semantic commitment as a dynamical process. We track class-conditional uncertainty along the denoising trajectory. Also, we show theoretically that the resulting transition region matches the speciation window predicted by high-dimensional symmetry-breaking analysis.

Physics perspective Several works characterize semantic emergence in diffusion sampling as a sharp high-dimensional transition, including the speciation instability of [Biroli et al. \(2024\)](#) and related symmetry-breaking and critical-window perspectives ([Raya & Ambrogioni, 2023](#); [Ambrogioni, 2025a](#); [Sclocchi et al., 2025](#); [Li & Chen, 2024](#)). These analyses provide mechanistic explanations but do not, in general, yield a simple online diagnostic for trained models or a direct prescription for time-localized intervention. Two notable steps toward practice are the work from [Pavasovic et al. \(2025\)](#), which leverages the high-dimensional regime picture to explain and improve classifier-free guidance, and from [Kynkänniemi et al. \(2024\)](#), which empirically shows that guidance is most beneficial when applied in a limited time interval. In contrast, we show theoretically that class-conditional entropy undergoes the same phase transition at the speciation time identified by [Biroli et al. \(2024\)](#) and provides a direct signature of the associated symmetry breaking. Moreover, being straightforward to estimate along the denoising trajectory, it offers a practically accessible diagnostic that can facilitate the adoption of physics-based insights in guided diffusion. By varying the semantic partition of the class space, our measures can resolve multiple branching events and levels of semantic structure, providing an adaptive and operational framework for analyzing generative dynamics in large-scale diffusion models.

3. Preliminaries

3.1. Diffusion Models

Diffusion models view data generation as a sequential stochastic transformation between two probability distributions: a complex data distribution and a simple noise distribution. This transformation is defined by stochastic differential equations (SDEs). The forward SDE gradually decreases information about the data by injecting noise, while the reverse SDE restores structure by progressively removing noise. Together, they form a continuous-time generative model in which each intermediate state X_t represents a partially noised version of the original data.

Formally, an SDE specifies how a random variable evolves with time:

$$dX_t = f(X_t, t) dt + g_t dW_t, \quad (1)$$

where W_t is a standard Wiener process, f is a drift field, and g is a time-dependent diffusion coefficient controlling the variance of the injected noise. The evolution of the marginal densities $p_t(x)$ is governed by the associated Fokker–Planck equation:

$$\partial_t p_t(x) = \sum_{j=1}^d \partial_{x_j} \left(-f_j(x, t) + \frac{g^2(t)}{2} \partial_{x_j} \right) p_t(x). \quad (2)$$

For many choices of (f, g) , the forward process admits a closed-form transition kernel $p_t(x|x_0)$, allowing us to efficiently sample noisy states without explicitly simulating the SDE. Examples of widely used SDEs are Variance-Preserving (VP) ([Song et al., 2021b](#)) and Elucidated Diffusion Models (EDM) ([Karras et al., 2022](#)).

The generative model is obtained by reversing the forward process. Under mild conditions, [Anderson \(1982\)](#) showed that reversing an SDE introduces an additional drift term involving the score $\nabla \log p_t(x)$:

$$dX_t = (f(X_t, t) - g_t^2 \nabla \log p_t(X_t)) dt + g_t d\widetilde{W}_t. \quad (3)$$

If the score were known exactly, sampling this reverse SDE (initialized from the approximately Gaussian final state of the forward process) would yield exact data samples. In practice, a neural network $s_\theta(x, t)$ is trained to approximate the score, which can then be used to numerically solve the reverse SDE to synthesize data.

To generate samples consistent with some label or prompt y , one replaces the unconditional score with the conditional score $\nabla_x \log p_t(x|y)$. In practice, techniques such as classifier guidance and classifier-free guidance are used ([Ho & Salimans, 2022](#); [Dhariwal & Nichol, 2021](#)).

3.2. Information Theory

Information theory provides a language for quantifying uncertainty and information flow in stochastic processes. In the context of diffusion models, the forward SDE can be interpreted as transmitting a data point through a progressively noisier channel, whereas the reverse SDE attempts to infer the original symbol from its corrupted versions. This perspective makes information-theoretic quantities natural tools for understanding how much of the original structure remains at different times t .

The fundamental measure of uncertainty is the (differential) entropy:

$$\mathbf{H}[X] = - \int p(x) \log p(x) dx. \quad (4)$$

Since our interest is in how much information about a variable is preserved as the diffusion process evolves, a central object is the *conditional entropy*:

$$\mathbf{H}[Y|X] = - \iint p(x, y) \log p(y|x) dx dy. \quad (5)$$

The conditional entropy quantifies the remaining uncertainty about Y given knowledge of X . When applied to diffusion trajectories, it captures how uncertainty about the underlying data or conditioning variable evolves as noise is added or removed.

4. Theoretical Analysis

In this section, we introduce our theoretical setup, motivate the usefulness of the class-conditional entropy, and derive a phase-transition result for its dynamics. For more details regarding the results in this section consult appendix A.

4.1. Problem Setup: Semantic Uncertainty

We consider a general diffusion forward process for which the transition kernel is Gaussian and isotropic:

$$p(x_t | x_0) = \mathcal{N}(x_t; \alpha_t x_0, \sigma_t^2 I_d), \quad (6)$$

with scalar schedules $\alpha_t \geq 0$ and $\sigma_t \geq 0$. This form covers commonly used SDE parameterizations (such as VP and EDM).

Let $Z \in \{1, \dots, N\}$ denote a latent semantic variable (e.g., a class label) with prior $p(Z = i)$, and let X_t be the noisy state at time t . Our goal is to track when semantics become ambiguous under the forward process (and, equivalently, when they become resolved along the reverse process). This can be quantified with the class-conditional entropy

$$\mathbf{H}[Z | X_t] = -\mathbb{E}_{x \sim p_t(\cdot)} \left[\sum_{k=1}^N \gamma_k(x, t) \log \gamma_k(x, t) \right], \quad (7)$$

where $\gamma_k(x, t) := \mathbb{P}(Z = k | X_t = x)$. Differentiating in t yields an expression for the instantaneous rate of information transfer, derived in Appendix A.1:

$$\dot{\mathbf{H}}[Z | X_t] = -\mathbb{E}_{i \sim p(\cdot)} \left[\frac{g_t^2}{2} \Delta_i(t) \right]. \quad (8)$$

where $\Delta_i(t)$ is the Fisher divergence between the class-conditional and unconditional marginal densities:

$$\Delta_i(t) := \mathbb{E}_{x \sim p_t(\cdot | i)} \left[\|\nabla_x \log p_t(x | i) - \nabla_x \log p_t(x)\|^2 \right] \quad (9)$$

Intuitively, large $\Delta_i(t)$ implies a large discrepancy between the score fields for $p_t(\cdot | Z = i)$ and $p_t(\cdot)$, suggesting that at noise level t the class identity remains discernable and has not yet merged into the unconditional distribution.

A complementary, more fine-grained view comes from pairwise class comparisons. For any two classes i and k , we define the log-posterior ratio

$$\Lambda_{ik}(x, t) := \log \frac{\gamma_i(x, t)}{\gamma_k(x, t)}. \quad (10)$$

This quantity is antisymmetric ($\Lambda_{ik} = -\Lambda_{ki}$) and can be read as a summary of how strongly x_t favors class i over k . Values near zero correspond to strong mixing between the two classes, while large values indicate that the two classes are well separated at noise level t . In the following, we show how these pairwise “mixing variables” control the entropy dynamics.

4.2. Gaussian Mixture

We now specialize to a finite, equiprobable Gaussian mixture prior p_0 in \mathbb{R}^d , with components indexed by $Z \in \{1, \dots, N\}$ and high-dimensional scaling $\|\mu_k\|^2/d = q_k$ and $\|\mu_k - \mu_i\|^2/d = \delta_{ik}^2$ for $i \neq k$ with $\sigma_0 = O(1)$.

Under the Gaussian kernel (6), each component remains Gaussian with time dependent mean and variance respectively $m_k(t) = \alpha_t \mu_k$ and $v(t) = \alpha_t^2 \sigma_0^2 + \sigma_t^2$. Accordingly, the component-wise posteriors are given by

$$\gamma_i(x, t) = \frac{\exp \left(-\frac{1}{2v(t)} \|x - m_i(t)\|^2 \right)}{\sum_{k=1}^N \exp \left(-\frac{1}{2v(t)} \|x - m_k(t)\|^2 \right)}. \quad (11)$$

In particular, fixing a reference class i , the posterior can be reparameterized in terms of the pairwise ratios (10) as

$$\gamma_i(x, t) = \frac{1}{1 + \sum_{k \neq i} e^{-\Lambda_{ik}(x, t)}}. \quad (12)$$

Conditioning x_t on $Z = i$, one finds that $\Lambda_{ik}(X_t, t)$ is Gaussian and admits the explicit decomposition

$$\Lambda_{ik}(X_t, t) = m_{ik}(t) + \sqrt{v_{ik}(t)} \epsilon, \quad \epsilon \sim \mathcal{N}(0, 1), \quad (13)$$

with mean $m_{ik}(t) := \frac{\|m_i(t) - m_k(t)\|^2}{2v(t)}$ and variance $v_{ik}(t) := \frac{\|m_i(t) - m_k(t)\|^2}{v(t)}$. Intuitively, $m_{ik}(t)$ measures the typical evidence favoring i over k , while $v_{ik}(t)$ quantifies how strongly this evidence fluctuates across samples at noise level t .

To evaluate the confidence of the pairwise decision i versus k , we use the effective signal-to-noise ratio

$$\text{SNR}_{ik}(t) := \frac{\|m_i(t) - m_k(t)\|^2}{4v(t)}. \quad (14)$$

When $\text{SNR}_{ik}(t)$ is large, Λ_{ik} is far from zero and the two classes are well separated, while when it is close to 0, the two classes are well mixed.

4.3. Speciation Time

We next specialize to the variance-preserving (VP) forward process, for which the Gaussian kernel takes the form $\alpha_t = e^{-t}$ and $\sigma_t^2 = 1 - e^{-2t}$ (equivalent to the setup in Biroli et al.

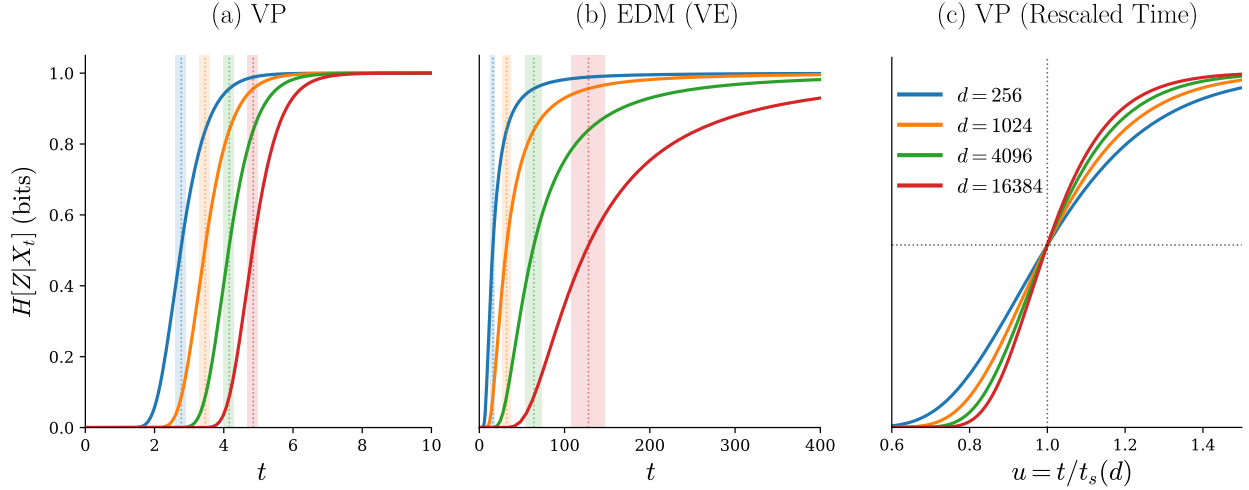


Figure 2. Class-conditional entropies $H[Z | X_t]$ for equi-probable two-component Gaussian mixture on different time scales for VP and VE kernels for several values of d . In (a) and (b) the conditional entropy using a VP and VE kernel respectively (i.e., $\alpha_t = e^{-t}$, $\sigma_t^2 = 1 - e^{-2t}$ and $\alpha_t = 1$, $\sigma_t^2 = \sigma_t^2$) in natural time t . In (c) the conditional entropy using a VP kernel in a time scale rescaled by $t_s = \frac{1}{2} \log d$. The vertical dotted lines indicate the speciation time t_s given by $\ln d/2$ and \sqrt{d} in VP and VE respectively, while the horizontal dotted line indicates convergence on the rescaled axis $u = t/t_s$.

(2024)). For our high-dimensional mixture assumptions we obtain the asymptotic scaling

$$\text{SNR}_{ik}(t) \asymp d \frac{e^{-2t}}{e^{-2t}\sigma_0^2 + 1 - e^{-2t}}. \quad (15)$$

A nontrivial transition occurs when signal and noise balance, i.e., when $\text{SNR}_{ik}(t)$ becomes $O(1)$ as $d \rightarrow \infty$. Solving for t yields the logarithmic speciation time scale

$$t_s = \frac{1}{2} \log d + O(1), \quad (16)$$

which matches the speciation time predicted by Biroli et al. (2024). On the rescaled variable $u = t/t_s$, the class-conditional entropy exhibits a sharp transition localized around $u \approx 1$, as illustrated in Figure 2 c.

Interestingly, the same sharp localization does not occur for variance-exploding (VE) / EDM-style forward processes. In that setting, $\alpha_t \equiv 1$ while σ_t grows with t , so the speciation time becomes some power of d^1 . Therefore, the SNR_{ik} does not have a sharp transition in u . At present, the practical significance of this difference is unclear. Understanding whether it has implications for schedulers or guidance remains an interesting direction for future work. The entropy profiles using both kernels are visualised for growing dimensions d in Figure 2.

¹Specifically for EDM, one has $\sigma_t = t$ and $t_s = \sqrt{d}$.

4.4. Hierarchical Branching

In realistic high-dimensional data distributions, different semantic distinctions are resolved at different stages of the diffusion process. Each such distinction corresponds to a local instability of the posterior along a specific class-separating direction of the form analyzed in Sec. 4.2, which, when considered in isolation, gives rise to its own speciation event. This motivates a hierarchical picture of semantic emergence, in which branching occurs at multiple levels of abstraction.

In the VP asymptotic regime, branching events do not remain well separated in time. Instead, they collapse into a narrow macroscopic transition region when observed through coarse quantities such as the class-conditional entropy or the order parameter studied in (Biroli & Mézard, 2023). As a result, although hierarchical branching exists at the level of individual pairwise distinctions, it is largely indistinguishable when viewed through global uncertainty measures. Moreover, the class-conditional entropy is insensitive to the specific content of the semantic structure that emerges, as illustrated in Figure 1.

Both limitations can be addressed by restricting the conditional entropy to subsets of classes, or more precisely, to non-exhaustive binary partitions of the class variable Z . This reduces the N -ary inference problem to a binary one and allows us to focus on specific class-separating distinctions defined by the log-posterior ratios in Eq. (10). We refer to the resulting quantity as the *partitioned class-conditional*

entropy:

$$\mathbf{H}[\pi(Z)|X_t] = -\mathbb{E}_{x \sim p_t^\pi(\cdot)} \left[\sum_{y \in \{0,1\}} \gamma_y(x, t) \log \gamma_y(x, t) \right], \quad (17)$$

where π is a Bernoulli random variable induced by a binary partition $(\mathcal{A}, \mathcal{B})$ of a subset of classes, with $\pi(Z) = \mathbf{1}_{\{Z \in \mathcal{A}\}}$, and γ_y denotes the corresponding renormalized posterior.

From the perspective developed above, the partitioned conditional entropy selectively probes a subset of log-posterior evidence variables while suppressing others. As a result, its temporal profile becomes sensitive to the specific time at which the corresponding semantic distinction becomes marginally reliable, i.e., when the associated evidence enters the $O(1)$ SNR regime. This provides a principled way to probe semantic distinctions at different levels of abstraction in trained diffusion models.

5. Numerical Experiments

In the following, we empirically analyze the partitioned class-conditional entropy and its temporal derivative along the reverse diffusion trajectory in trained models. The experiments were conducted using EDM2-XS and Stable Diffusion 1.5, trained on ImageNet-512 and LAION-5B, respectively. Entropy profiles are estimated using the online posterior-tracking procedure described in Section 5.1, with further experimental details reported in Appendix C.

5.1. Estimating the Entropy in Trained Models

In trained diffusion models, the posteriors are not available in closed form. To estimate the partitioned conditional entropy $H[\pi(Z)|X_t]$ along the denoising trajectory, we therefore adopt an online posterior-tracking procedure that takes advantage of the Markov structure of the forward diffusion process and the availability of conditional and unconditional models (Koulischer et al., 2025a). This allows us to propagate class posteriors backward along a denoising trajectory by iteratively updating log-posterior ratios using local likelihood increments between successive noise levels.

Concretely, for a given semantic partition, we estimate the posterior $\gamma_\pi(x_t)$ by accumulating the log-likelihood ratio between the conditional and reference denoisers. At each time step, the update is expressed in terms of squared reconstruction errors, which can be computed directly from the model’s noise or data predictions (Algorithm 2 in Koulischer et al. (2025a)). The partitioned conditional entropy is then obtained by Monte Carlo averaging over the sampled trajectories. Algorithm 1 summarizes the procedure with further details being discussed in Appendix B.

Algorithm 1 Estimating $\mathbf{H}[\pi(Z)|X_t]$

```

1: Input: Conditional Denoiser  $D_\theta$ ,  $N$ ,  $\tau$ 
2: Sample  $x_\tau^{(0)}, x_\tau^{(1)}$  from  $p_\tau$ 
3:  $H_\tau \leftarrow 1$ 
4: for  $y \in \{0, 1\}$  do
5:   Initialize  $\gamma_y \leftarrow 0.5$ 
6:   for  $t = \tau, \tau - 1, \dots, 1$  do
7:      $x_{t-1}^{(y)} \leftarrow \text{sample}(y, D_\theta, x_t^{(y)}, t)$ 
8:      $\gamma_y \leftarrow \text{update\_posterior}(\gamma_y, D_\theta, x_t^{(y)}, x_{t-1}^{(y)}, t)$ 
9:      $h \leftarrow \gamma_y \log \gamma_y + (1 - \gamma_y) \log(1 - \gamma_y)$ 
10:     $I_{t-1}^{(y)} \leftarrow \frac{0.5}{N} \sum_{i=1}^N h^{(i)}$ 
11:   end for
12:    $H_{\tau-1:0} \leftarrow I_{\tau-1:0}^{(0)} + I_{\tau-1:0}^{(1)}$ 
13: end for
14: Output:  $H_{\tau:0}$ 

```

5.2. EDM2-XS

On ImageNet, we approximate Eq. (17) using binary partitions of the label space, separating each class from its complement. This produces class-specific entropy profiles that determine when semantic structure distinguishes a given class from the remainder of the dataset during the reverse process. For simplicity, we use the unconditional model as a proxy for $\nabla_x \log p_t(x|Z \neq i)$ which allows the expectation in Eq. (17) to be split into tractable terms. We also identify empirically optimal guidance intervals using FID (Heusel et al., 2017) and FD_{DINOv2} (Stein et al., 2023), following (Kynkänniemi et al., 2024) (Appendix C) to study the change in information transfer by comparing the no-guidance profiles with their FID and FD_{DINOv2} optimal counterparts.

Class-specific feature emergence Consistent with the theoretical analysis in Section 4, we find that the entropy production is confined to a narrow interval in the intermediate stages of diffusion (Figure 1). A non-zero \dot{H} indicates regimes in which class posteriors fluctuate across samples, i.e., where semantic commitment is being resolved. Empirically, most classes exhibit a similar uni modal profile centered around a common noise range, supporting previous claims of time-localized structure generation (Sclocchi et al., 2025; Li & Chen, 2024). At the same time, there are systematic class-dependent deviations in the location and shape of this window. For example, *tiger shark* exhibits an entropy production profile that is shifted toward higher noise levels and sustained over a broader interval, whereas *paintbrush* peaks at substantially lower noise. This indicates that different classes resolve their defining semantics at different effective noise scales. In particular, peaks at high noise levels are consistent with semantics that are captured by coarse, low-order statistics of the conditional distribution,

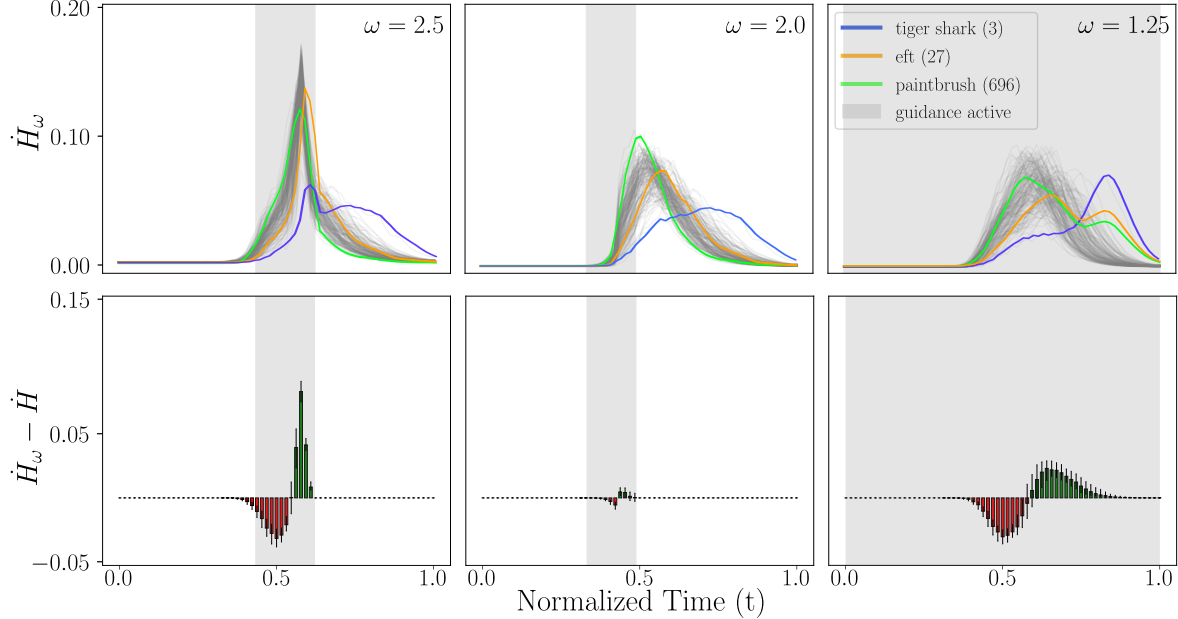


Figure 3. Overview of information distortion caused by optimal guidance on ImageNet. (Top) Class-conditional entropy production profiles when guidance with scale ω is applied within the gray interval. From left to right, intervals and guidance scales are optimized with respect to $\text{FD}_{\text{DINOv2}}$ (limited interval), FID (limited interval), and $\text{FD}_{\text{DINOv2}}$ with guidance applied throughout the full denoising trajectory. (Bottom) Difference between the guided entropy production \dot{H}_ω and the unguided baseline \dot{H} (Figure 1), summarized by the median and the 25th and 75th percentiles across classes. Green bars indicate an increase in entropy production relative to the baseline, while red bars indicate a reduction.

while peaks at lower noise levels suggest reliance on higher-frequency, fine-grained structure which is supported by the denoised predictions shown in the lower half of Figure 1 and additional examples provided in Appendix C.1.

Information distortion under guidance When using guidance, the entropy production \dot{H}_ω is systematically redistributed along the denoising trajectory relative to the unguided baseline (Figure 3). Guidance restricted to the $\text{FD}_{\text{DINOv2}}$ -optimal interval shifts entropy production toward higher noise levels and suppresses it at lower ones, causing \dot{H}_ω to peak sooner. This indicates that semantic commitment is enforced earlier in the reverse process aligning with the theoretical picture in Section 4.2. When guidance is applied within the FID -optimal interval (center column), it induces only small distortions of \dot{H} , limited to low-noise regimes where entropy production has already collapsed. Thus, it mainly affects feature refinement rather than semantic decision making. Applied throughout the entire trajectory (right column), guidance produces a pronounced shift of entropy production toward high-noise stages. The corresponding information shift remains relatively uniform, consistent with a gradual denoising of coarse, low-frequency structure rather than a sharp semantic transition. This redistribution is most pronounced for classes whose unguided entropy production overlaps with the guided interval, such as *tiger shark*, and largely absent for classes whose en-

tropy production is mainly limited to low noise levels. In Appendix C.1, we provide generated images as well as predicted noiseless trajectories of the form in Figure 1 for the highlighted classes when applying optimal guidance in the respective intervals.

5.3. Stable Diffusion 1.5

In ImageNet, the emergence of semantic structure can only be probed at the abstraction level defined by the latent class variable. Therefore, the interpretation of the corresponding entropy profiles remains agnostic to finer semantic attributes within a class. Text-conditioned diffusion models provide a substantially more informative semantic variable, enabling the estimation of Eq. (17) for partitions that target specific and localized semantic content. In these settings, the entropy can be interpreted as a measure of the overlap between the marginal distributions of two prompts, with high and low overlap corresponding to high and low entropy, respectively. This overlap diminishes as semantic differences between the prompts are resolved during the reverse process, thereby isolating the temporal window in which the variant-specific feature emerges. To measure the emergence of specific attributes, we consider base prompts together with minimally modified variants designed to introduce semantic differences at different levels of abstraction.

Figure 4 shows representative entropy profiles for four

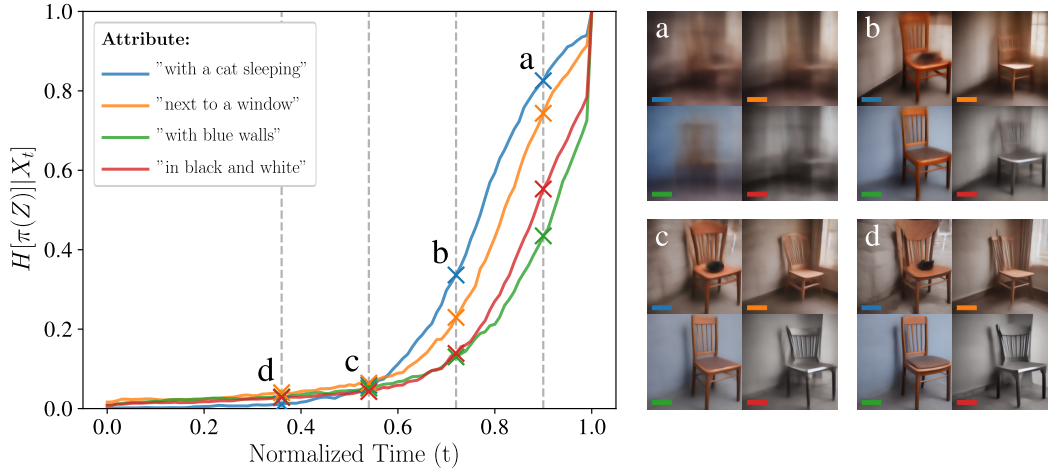


Figure 4. Entropy profiles for binary partitions of the form: “A wooden chair” vs. “A wooden chair + attribute”. (Left) Profiles computed along the mixture distribution show that low-frequency changes (e.g., color) exhibit sharper entropy decay at higher noise levels. (Right) Samples with shared initial conditions confirm earlier generation of low-frequency details (blue walls) versus high-frequency elements (cat), with semantic commitment coinciding with entropy collapse.

prompt variants that target semantic attributes at different spatial and spectral scales. Low-frequency decisions, such as global color changes (e.g., “*with blue walls*” or “*in black and white*”), exhibit an early and rapid entropy decay, indicating semantic commitment at high noise levels. In contrast, localized, high-frequency attributes, such as the presence of a *cat* or a *window*, show a slower entropy collapse, consistent with semantic resolution at later stages of denoising. Figure 4 visualizes this correspondence by showing noiseless predictions at selected timesteps for each variant. In snapshot (a), decisions regarding the blue walls and the black-and-white aesthetics appear resolved, while substantial ambiguity remains over the window and the cat. In (b), both low-frequency components are fully determined and the window structure begins to emerge. Only in (c) have all semantic decisions been made, as reflected by the collapse of all entropy profiles. Additional examples for the same base prompt and other prompt configurations are provided and discussed in Appendix C.2.

6. Limitations and Future Work

Our analysis relies on an online posterior update mechanism that compares conditional and reference noise predictions using local likelihood increments. Its accuracy depends on the calibration of these predictions across noise levels. Systematic prediction errors can bias posterior updates and distort entropy profiles, particularly when models are probed out of distribution. In the ImageNet setting, where the class space is well defined, using the unconditional model as a proxy for the class complement provides a stable estimator in practice. However, this approximation can introduce bias when the proxy deviates from the true complement distribution.

For Stable Diffusion 1.5, the present experiments are further limited by the model’s ability to generate fine-grained detail. Prompt modifications can induce larger distributional shifts than intended, complicating the isolation of individual semantic attributes. Extending the analysis to stronger and better-aligned models, such as Stable Diffusion XL or Stable Diffusion 3, is therefore a natural next step (Rombach et al., 2022; Esser et al., 2024). More broadly, future work should explore the use of external models trained to detect specific features as part of the estimation pipeline. Finally, a more formal characterization of how guidance controls the magnitude and timing of entropy redistribution along the sampling trajectory remains an open problem.

7. Conclusion

We introduced class-conditional entropy and its temporal derivative as practical tools for analyzing semantic emergence in diffusion models. In high-dimensional Gaussian mixtures, we showed that entropy production concentrates on the same logarithmic time scale as the speciation instability predicted by statistical physics, linking symmetry breaking to an information-theoretic measure of uncertainty. Experiments on EDM2-XS and Stable Diffusion 1.5 demonstrate that partitioned entropy reliably localizes the noise regimes in which semantic distinctions are resolved and provides a quantitative view of how guidance redistributes semantic information over time, consistent with recent findings on its time-dependent effectiveness (Kynkänniemi et al., 2024). Together, these results connect information-theoretic and dynamical perspectives on diffusion and offer a principled diagnostic for time-localized analysis of guided generative models.

Impact statement

This paper presents work whose goal is to advance the field of machine learning. There are many potential societal consequences of our work, none of which we feel must be specifically highlighted here.

References

Ambrogioni, L. The statistical thermodynamics of generative diffusion models: Phase transitions, symmetry breaking, and critical instability. *Entropy*, 27(3):291, 2025a.

Ambrogioni, L. The information dynamics of generative diffusion, 2025b.

Anderson, B. D. Reverse-time diffusion equation models. *Stochastic Processes and their Applications*, 1982.

Betker, J., Goh, G., Jing, L., Brooks, T., Wang, J., Li, L., Ouyang, L., Zhuang, J., Lee, J., Guo, Y., Manassra, W., Dhariwal, P., Chu, C., Jiao, Y., Ramesh, A., et al. Improving image generation with better captions. Technical report, OpenAI, 2023. URL <https://cdn.openai.com/papers/dall-e-3.pdf>.

Biroli, G. and Mézard, M. Generative diffusion in very large dimensions. *Journal of Statistical Mechanics: Theory and Experiment*, 2023.

Biroli, G., Bonnaire, T., de Bortoli, V., and Mézard, M. Dynamical regimes of diffusion models. *Nature Communications*, 15(1), 2024.

Deng, J., Socher, R., Fei-Fei, L., Dong, W., Li, K., and Li, L.-J. Imagenet: A large-scale hierarchical image database. In *2009 IEEE Conference on Computer Vision and Pattern Recognition(CVPR)*, 2009.

Dhariwal, P. and Nichol, A. Q. Diffusion models beat GANs on image synthesis. In *Advances in Neural Information Processing Systems*, 2021.

Esser, P., Kulal, S., Blattmann, A., Entezari, R., Müller, J., Saini, H., Levi, Y., Lorenz, D., Sauer, A., Boesel, F., Podell, D., Dockhorn, T., English, Z., and Rombach, R. Scaling rectified flow transformers for high-resolution image synthesis. In *Proceedings of the 41st International Conference on Machine Learning*, ICML'24. JMLR.org, 2024.

Franzese, G., Bounoua, M., and Michiardi, P. MINDE: Mutual information neural diffusion estimation. In *The Twelfth International Conference on Learning Representations*, 2024.

Heusel, M., Ramsauer, H., Unterthiner, T., Nessler, B., and Hochreiter, S. Gans trained by a two time-scale update rule converge to a local nash equilibrium. In *Advances in Neural Information Processing Systems*, 2017.

Ho, J. and Salimans, T. Classifier-free diffusion guidance. *CoRR*, abs/2207.12598, 2022.

Ho, J., Jain, A., and Abbeel, P. Denoising diffusion probabilistic models. 2020.

Karras, T., Aittala, M., Aila, T., and Laine, S. Elucidating the design space of diffusion-based generative models. In *Advances in Neural Information Processing Systems*, 2022.

Karras, T., Aittala, M., Lehtinen, J., Hellsten, J., Aila, T., and Laine, S. Analyzing and improving the training dynamics of diffusion models. In *Proc. CVPR*, 2024.

Kong, X., Brekelmans, R., and Steeg, G. V. Information-theoretic diffusion. In *The Eleventh International Conference on Learning Representations*, 2023.

Kong, X., Liu, O., Li, H., Yogatama, D., and Steeg, G. V. Interpretable diffusion via information decomposition. In *The Twelfth International Conference on Learning Representations*, 2024.

Kong, Z., Ping, W., Huang, J., Zhao, K., and Catanzaro, B. Diffwave: A versatile diffusion model for audio synthesis. In *International Conference on Learning Representations*, 2021.

Koulischer, F., Deleu, J., Raya, G., Demeester, T., and Ambrogioni, L. Dynamic negative guidance of diffusion models. In *The Thirteenth International Conference on Learning Representations*, 2025a.

Koulischer, F., Handke, F., Deleu, J., Demeester, T., and Ambrogioni, L. Feedback guidance of diffusion models. In *The Thirty-ninth Annual Conference on Neural Information Processing Systems*, 2025b.

Kynkänniemi, T., Aittala, M., Karras, T., Laine, S., Aila, T., and Lehtinen, J. Applying guidance in a limited interval improves sample and distribution quality in diffusion models. In *Advances in Neural Information Processing Systems*, volume 37, 2024.

Kynkänniemi, T., Karras, T., Laine, S., Lehtinen, J., and Aila, T. Improved precision and recall metric for assessing generative models. *CoRR*, 2019.

Li, M. and Chen, S. Critical windows: non-asymptotic theory for feature emergence in diffusion models. 2024.

Montanari, A. Sampling, diffusions, and stochastic localization. *arXiv preprint arXiv:2305.10690*, 2023.

Montanari, A. and Wu, Y. Posterior sampling in high dimension via diffusion processes. *arXiv preprint arXiv:2304.11449*, 2023.

Nichol, A. Q., Dhariwal, P., Ramesh, A., Shyam, P., Mishkin, P., McGrew, B., Sutskever, I., and Chen, M. GLIDE: Towards photorealistic image generation and editing with text-guided diffusion models. In *Proceedings of the 39th International Conference on Machine Learning*, 2022.

Oquab, M., Darcet, T., Moutakanni, T., Vo, H. V., Szafraniec, M., Khalidov, V., Fernandez, P., HAZIZA, D., Massa, F., El-Nouby, A., Assran, M., Ballas, N., Galuba, W., Howes, R., Huang, P.-Y., Li, S.-W., Misra, I., Rabbat, M., Sharma, V., Synnaeve, G., Xu, H., Jegou, H., Mairal, J., Labatut, P., Joulin, A., and Bojanowski, P. DINOv2: Learning robust visual features without supervision. *Transactions on Machine Learning Research*, 2024. ISSN 2835-8856. Featured Certification.

Pavasovic, K. L., Verbeek, J., Biroli, G., and Mezard, M. Understanding classifier-free guidance: High-dimensional theory and non-linear generalizations, 2025.

Premkumar, A. Neural entropy. In *The Thirty-ninth Annual Conference on Neural Information Processing Systems*, 2025.

Premkumar, A. Diffusion models are kelly gamblers. ICLR 2026 Conference Submission, 2026.

Ramesh, A., Dhariwal, P., Nichol, A., Chu, C., and Chen, M. Hierarchical text-conditional image generation with clip latents. Technical report, OpenAI, 2022. URL <https://cdn.openai.com/papers/dall-e-2.pdf>.

Raya, G. and Ambrogioni, L. Spontaneous symmetry breaking in generative diffusion models. In *Advances in Neural Information Processing Systems*, 2023.

Rombach, R., Blattmann, A., Lorenz, D., Esser, P., and Ommer, B. High-resolution image synthesis with latent diffusion models. In *Proceedings of the IEEE/CVF Conference on Computer Vision and Pattern Recognition (CVPR)*, 2022.

Saharia, C., Chan, W., Saxena, S., Li, L., Whang, J., Denton, E. L., Seyed Ghasemipour, S. K., Ayan, B. K., Mahdavi, S. S., Gontijo Lopes, R., Salimans, T., Ho, J., Fleet, D. J., and Norouzi, M. Photorealistic text-to-image diffusion models with deep language understanding. In *Advances in Neural Information Processing Systems*, 2022.

Sajjadi, M. S. M., Bachem, O., Lucic, M., Bousquet, O., and Gelly, S. Assessing generative models via precision and recall. In *Advances in Neural Information Processing Systems*.

Schuhmann, C., Beaumont, R., Vencu, R., Gordon, C. W., Wightman, R., Cherti, M., Coombes, T., Katta, A., Mullis, C., Wortsman, M., Schramowski, P., Kundurthy, S. R., Crowson, K., Schmidt, L., Kaczmarczyk, R., and Jitsev, J. LAION-5b: An open large-scale dataset for training next generation image-text models. In *Thirty-sixth Conference on Neural Information Processing Systems Datasets and Benchmarks Track*, 2022.

Sclocchi, A., Favero, A., and Wyart, M. A phase transition in diffusion models reveals the hierarchical nature of data. *Proceedings of the National Academy of Sciences*, 2025.

Singer, U., Polyak, A., Hayes, T., Yin, X., An, J., Zhang, S., Hu, Q., Yang, H., Ashual, O., Gafni, O., Parikh, D., Gupta, S., and Taigman, Y. Make-a-video: Text-to-video generation without text-video data. In *The Eleventh International Conference on Learning Representations*, 2023.

Sohl-Dickstein, J., Weiss, E., Maheswaranathan, N., and Ganguli, S. Deep unsupervised learning using nonequilibrium thermodynamics. In *ICML*, 2015.

Song, J., Meng, C., and Ermon, S. Denoising diffusion implicit models. In *International Conference on Learning Representations*, 2021a.

Song, Y., Sohl-Dickstein, J., Kingma, D. P., Kumar, A., Ermon, S., and Poole, B. Score-based generative modeling through stochastic differential equations. In *International Conference on Learning Representations*, 2021b.

Stancevic, D., Handke, F., and Ambrogioni, L. Entropic time schedulers for generative diffusion models. In *Advances in Neural Information Processing Systems*, 2025.

Stein, G., Cresswell, J. C., Hosseinzadeh, R., Sui, Y., Ross, B. L., Villecroze, V., Liu, Z., Caterini, A. L., Taylor, E., and Loaiza-Ganem, G. Exposing flaws of generative model evaluation metrics and their unfair treatment of diffusion models. In *Thirty-seventh Conference on Neural Information Processing Systems*, 2023.

Szegedy, C., Vanhoucke, V., Ioffe, S., Shlens, J., and Wojna, Z. Rethinking the inception architecture for computer vision. In *CVPR*, pp. 2818–2826, 2016.

Wang, C., Franzese, G., Finamore, A., Gallo, M., and Michiardi, P. Information theoretic text-to-image alignment. In *International Conference on Learning Representations*, 2025.

A. Asymptotic analysis of the class-conditional entropy for a mixture of Gaussians

As stated in the main text, the class-conditional entropy experiences a phase transition over an $O(1)$ interval at the speciation time only for the VP SDE and fails for the VE (and EDM) SDEs. Here, we provide a proof of this claim by inspecting how the entropy production behaves.

A.1. Conditional entropy production

Here, we derive the result given in Eq. (8). We can rewrite the class-conditional entropy as

$$\mathbf{H}[Z|X_t] = \mathbf{H}(Z) - \mathbf{I}[X_t; Z] = \mathbf{H}[Z] - \mathbf{H}[X_t] + \mathbf{H}[X_t|Z]$$

Taking the derivative with respect to t time eliminates $\mathbf{H}[Z]$. Furthermore, $\mathbf{H}[X_t]$ and $\mathbf{H}[X_t|Z]$ are equivalent in form:

$$\begin{aligned}\dot{\mathbf{H}}[X_t|Z] &= - \sum_{i=1}^N p(Z=i) \frac{d}{dt} \int p_t(x|Z=i) \log p_t(x|Z=i) dx \\ &= \sum_{i=1}^N p(Z=i) \dot{\mathbf{H}}[X_t|Z=i] \\ \dot{\mathbf{H}}[X_t|Z=i] &= - \int \dot{p}_t(x|Z=i) \log p_t(x|Z=i) dx.\end{aligned}$$

Assuming that the process is described by Eq. (1), we can further simplify using the Fokker-Planck equation in forward time (Anderson, 1982):

$$\begin{aligned}\dot{\mathbf{H}}[X_t|Z=i] &= - \int -\nabla \left[\left(f_t - \frac{g_t^2}{2} \nabla \log p_t(x|Z=i) \right) p_t(x|Z=i) \right] \log p_t(x|Z=i) dx \\ &= - \int \left\langle f_t - \frac{g_t^2}{2} \nabla \log p_t(x|Z=i) \mid \nabla \log p_t(x|Z=i) \right\rangle p_t(x|Z=i) dx \\ &= - \int \langle f_t \mid \nabla \log p_t(x|Z=i) \rangle p_t(x) dx + \int \frac{g_t^2}{2} \langle \nabla \log p_t(x|Z=i) \mid \nabla \log p_t(x|Z=i) \rangle p_t(x) dx \\ &= \int p_t(x|Z=i) \nabla(f_t) dx + \frac{g_t^2}{2} \int p_t(x|Z=i) \|\nabla \log p_t(x|Z=i)\|^2 dx \\ &= \mathbb{E}_{x \sim p_t(\cdot|Z=i)} [\nabla(f_t)] + \frac{g_t^2}{2} \mathbb{E}_{x \sim p_t(\cdot|Z=i)} [\|\nabla \log p_t(x|Z=i)\|^2] \\ \dot{\mathbf{H}}[X_t] &= \mathbb{E}_{x \sim p_t(\cdot)} [\nabla(f_t)] + \frac{g_t^2}{2} \mathbb{E}_{x \sim p_t(\cdot)} [\|\nabla \log p_t(x)\|^2].\end{aligned}$$

Therefore:

$$\begin{aligned}\dot{\mathbf{H}}[Z|X_t] &= \dot{\mathbf{H}}[X_t|Z] - \dot{\mathbf{H}}[X_t] \\ &= \frac{g_t^2}{2} \mathbb{E}_{x,i \sim p_t(\cdot,\cdot)} [\|\nabla \log p_t(x|Z=i)\|^2 - \|\nabla \log p_t(x)\|^2] \\ &= \frac{g_t^2}{2} \mathbb{E}_{x,i \sim p_t(\cdot,\cdot)} [\|\nabla \log p_t(x|Z=i) - \nabla \log p_t(x)\|^2]\end{aligned}\tag{18}$$

A.2. Speciation time

We introduce the general setup for the mixture of Gaussians and show how the speciation time is defined for the conditional entropy. Then we specialize to the VP and EDM cases.

A.2.1. SETUP

Assume a Gaussian forward kernel

$$p(x_t \mid x_0) = \mathcal{N}(x_t; \alpha_t x_0, \sigma_t^2 I_d),\tag{19}$$

and an equiprobable Gaussian mixture prior

$$p_0(x) = \frac{1}{N} \sum_{k=1}^N \mathcal{N}(x; \mu_k, \sigma_0^2 I_d). \quad (20)$$

We assume that means and variances scale as $\|\mu_k\|^2/d = q_k$, $\|\mu_k - \mu_i\|^2/d = \delta_{ik}^2$ for $i \neq k$, and $\sigma_0 = O(1)$. Then $X_t | (Z = k) \sim \mathcal{N}(m_k(t), v(t)I_d)$ with

$$m_k(t) = \alpha_t \mu_k, \quad v(t) = \alpha_t^2 \sigma_0^2 + \sigma_t^2. \quad (21)$$

In the rest of the proof, we focus on the behavior of entropy production and from there we can easily draw conclusion about the class-conditional entropy. From previous section we have

$$\dot{\mathbf{H}}[Z|X_t] = \mathbb{E}[\Delta_i(t)], \quad (22)$$

where

$$\Delta_i(t) := \mathbb{E}[\|s_i(X_t, t) - s_{\text{mix}}(X_t, t)\|^2 | Z = i]. \quad (23)$$

The component score field is

$$s_k(x, t) := \nabla_x \log p(x | Z = k) = -\frac{1}{v(t)}(x - m_k(t)), \quad (24)$$

and the mixture score satisfies the standard identity

$$s_{\text{mix}}(x, t) := \nabla_x \log p_t(x) = \sum_{k=1}^N \gamma_k(x, t) s_k(x, t) = -\frac{1}{v(t)} \left(x - \sum_{k=1}^N \gamma_k(x, t) m_k(t) \right), \quad (25)$$

where the mixture posterior is given by

$$\gamma_k(x, t) = \mathbb{P}(Z = k | X_t = x) = \frac{\exp\left(-\frac{1}{2v(t)}\|x - m_k(t)\|^2\right)}{\sum_{\ell=1}^N \exp\left(-\frac{1}{2v(t)}\|x - m_\ell(t)\|^2\right)}. \quad (26)$$

For a fixed class i , we get

$$\|s_i(x, t) - s_{\text{mix}}(x, t)\|^2 = \frac{1}{v(t)^2} \left\| m_i(t) - \sum_{k=1}^N \gamma_k(x, t) m_k(t) \right\|^2. \quad (27)$$

To ease our analysis, we rewrite the posteriors as follows

$$\gamma_i(x, t) = \frac{1}{1 + \sum_{k \neq i} e^{-\Lambda_{ik}(x, t)}}, \quad \gamma_k(x, t) = \frac{e^{-\Lambda_{ik}(x, t)}}{1 + \sum_{\ell \neq i} e^{-\Lambda_{i\ell}(x, t)}} \quad (k \neq i), \quad (28)$$

where $\Lambda_{ik}(x, t) := \log \frac{\gamma_i(x, t)}{\gamma_k(x, t)}$.

Or by inserting the expressions for posteriors:

$$\Lambda_{ik}(x, t) = \frac{\|x - m_k(t)\|^2 - \|x - m_i(t)\|^2}{2v(t)} \quad (29)$$

$$= \frac{\|x\|^2 - 2xm_k(t) + \|m_k(t)\|^2 - \|x\|^2 + 2xm_i(t) - \|m_i(t)\|^2}{2v(t)} \quad (30)$$

$$= \frac{\|m_k(t)\|^2 - \|m_i(t)\|^2 + 2x(m_i(t) - m_k(t))}{2v(t)} \quad (31)$$

$$(32)$$

Condition on $Z = i$ and write

$$X_t = m_i(t) + \sqrt{v(t)} \varepsilon, \quad \varepsilon \sim \mathcal{N}(0, I_d). \quad (33)$$

For $k \neq i$, define $\Delta_{ik}(t) := m_i(t) - m_k(t) = e^{-t}(\mu_i - \mu_k)$. Then

$$\Lambda_{ik}(x, t) = \frac{\|m_k(t)\|^2 - \|m_i(t)\|^2 + 2(m_i(t) + \sqrt{v(t)}\varepsilon)(m_i(t) - m_k(t))}{2v(t)} \quad (34)$$

$$= \frac{\|m_k(t)\|^2 - 2m_i(t)m_k(t) + \|m_i(t)\|^2 + 2\sqrt{v(t)}(m_i(t) - m_k(t))\varepsilon}{2v(t)} \quad (35)$$

$$= \frac{\|\Delta_{ik}(t)\|^2}{2v(t)} + \frac{1}{\sqrt{v(t)}} \Delta_{ik}(t)^\top \varepsilon, \quad (36)$$

(37)

Hence, $\Lambda_{ik} \mid (Z = i)$ is Gaussian with mean $m_{ik}(t) = \|\Delta_{ik}(t)\|^2/(2v(t))$ and variance $v_{ik}(t) = \|\Delta_{ik}(t)\|^2/v(t)$.

We define the speciation scale by the condition $\frac{\|\Delta_{ik}(t)\|^2}{v(t)} = O(1)$.

A.2.2. VP CASE

For the variance-preserving OU process, $\alpha_t = e^{-t}$ and $\sigma_t^2 = 1 - e^{-2t}$, so $v(t) = e^{-2t}\sigma_0^2 + (1 - e^{-2t})$, we have

$$4\text{SNR}_{ik}(t) = \frac{\|e^{-t}(\mu_i - \mu_k)\|^2}{e^{-2t}\sigma_0^2 + (1 - e^{-2t})}. \quad (38)$$

Under the high-dimensional scaling $\|\mu_i - \mu_k\|^2 \asymp d$, this simplifies to

$$\text{SNR}_{ik}(t) \asymp d \frac{e^{-2t}}{e^{-2t}\sigma_0^2 + 1 - e^{-2t}}. \quad (39)$$

It is easy to see that

$$t_s = \frac{1}{2} \log d + O(1). \quad (40)$$

satisfies $\text{SNR}_{ik}(t_s) = O(1)$ as $d \rightarrow \infty$. Then we can write $e^{-2t} = e^{-2ut_s} = d^{-u}$.

Now, we explore how $\Delta_i(t)$ behaves at different times as $d \rightarrow \infty$. First, let us express the means and variances in terms of u as follows

$$m_i(u) = d^{-\frac{u}{2}} \mu_i, \quad v(u) = d^{-u}(\sigma_0^2 - 1) + 1, \quad (41)$$

and Λ_{ik} as

$$\Lambda_{ik}(X_t, u) = \frac{\|\mu_i - \mu_k\|^2}{2((\sigma_0^2 - 1) + d^u)} + \frac{1}{\sqrt{((\sigma_0^2 - 1) + d^u)}} \|\mu_i - \mu_k\|^\top \varepsilon. \quad (42)$$

Hence, we can see that for a fixed $u > 0$ as $d \rightarrow \infty$ we have

$$m_{ik}(u) \asymp d^{1-u}, \quad v_{ik}(u) \asymp d^{1-u}. \quad (43)$$

For $u > 1$, $d^{1-u} \rightarrow 0$ implying $m_{ik} \rightarrow 0$ with variance going to zero as well. Hence, $\gamma_k(x, u) \rightarrow \frac{1}{N}$ and

$$\Delta_i(u) \asymp d^{1-u} \rightarrow 0.$$

For $u < 1$, $d^{1-u} \rightarrow \infty$ implying $m_{ik} \rightarrow \infty$ with variance going to infinity as well. However, since the standard deviation grows as $d^{\frac{1-u}{2}}$, fluctuations of Λ_{ik} around its mean are of the same order of magnitude implying

$$\gamma_i(x, t) \rightarrow 1, \quad \gamma_k(x, t) \rightarrow 0 \quad (k \neq i).$$

Hence, $\Delta_i(u) \rightarrow 0$.

At $u = 1$, we infer that there is a spike in the entropy production, since we know that the conditional entropy equals zero at the beginning and approximately equals $\ln(N)$ at the end of diffusion.

This shows that there is a phase transition in the conditional entropy over time scales of order $t_s(d) = \frac{\ln d}{2}$, which is exactly the speciation time in [Biroli et al. \(2024\)](#). Hence, by looking at the peaks of the conditional entropy production, we should be able to detect the speciation time.

A.2.3. EDM CASE

Now, we consider the EDM SDE

$$dX_t = \sqrt{2t} dW_t. \quad (44)$$

The solution is given by

$$X_t = X_0 + t \varepsilon, \quad \varepsilon \sim \mathcal{N}(0, I_d), \quad \varepsilon \perp X_0. \quad (45)$$

Hence,

$$X_t \mid (Z = i) \sim \mathcal{N}\left(m_i(t), v(t)I_d\right), \quad m_i(t) := \mu_i, \quad v(t) := \sigma_0^2 + t^2. \quad (46)$$

Using the same setup as for the VP case, we can repeat the same calculations to get

$$\Lambda_{ik}(X_t, t) = \frac{\|\Delta_{ik}(t)\|^2}{2v(t)} + \frac{1}{\sqrt{v(t)}} \Delta_{ik}(t)^\top \varepsilon, \quad (47)$$

where, again, $\Delta_{ik} = m_i(t) - m_k(t)$. However, in this case the speciation time is defined as

$$t_s(d) := \sqrt{d} \quad u = \frac{t}{t_s(d)}. \quad (48)$$

Now, it is easy to see that, for a fixed $u > 0$ as $d \rightarrow \infty$, we have

$$m_{ik}(u) \asymp u^{-2}, \quad v_{ik}(u) \asymp u^{-2}. \quad (49)$$

Therefore, the entropy depends on the dimension d only implicitly through the rescaled time variable $u = \frac{t}{t_s(d)}$. As a consequence, there is no sharp transition of the class-conditional entropy in u , and, as d increases, the mixing region broadens and scales with \sqrt{d} , rather than remaining of constant finite width as in the VP SDE. This difference between two SDEs is shown in figure 5.

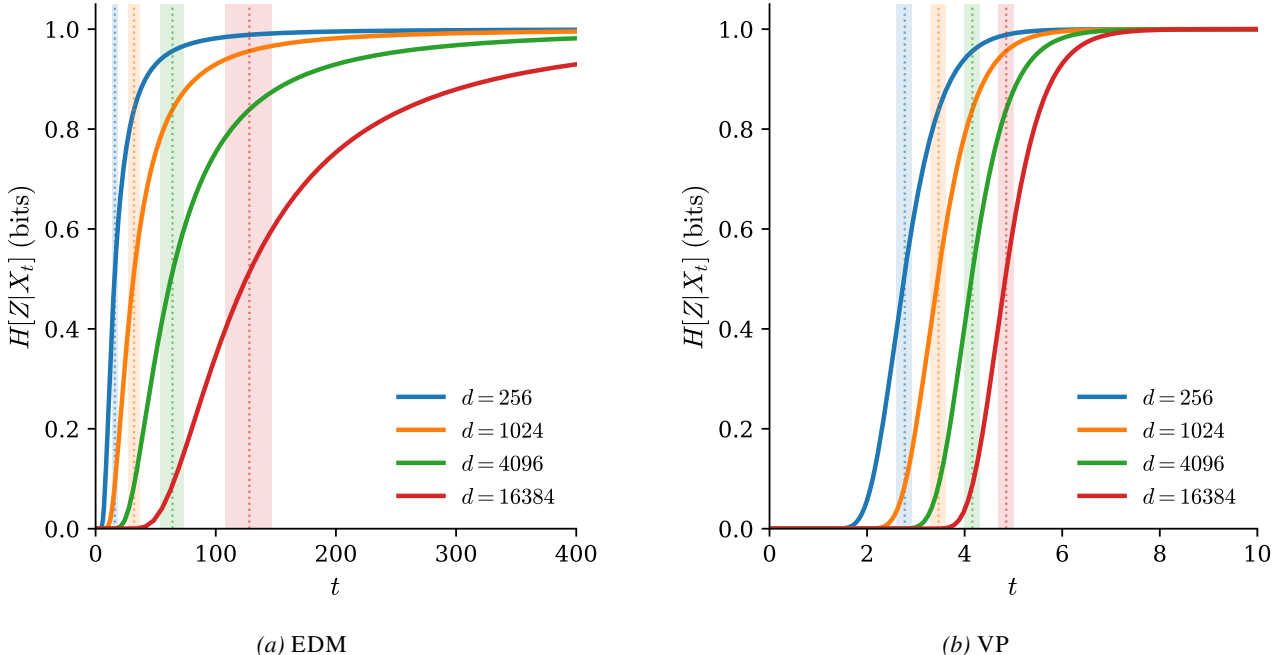


Figure 5. Class-conditional entropy $H[Z \mid X_t]$ against time t for equiprobable two-component Gaussian mixtures, for the EDM (left) and VP (right) forward SDEs and several values of d . Shaded vertical regions represent time intervals for which entropy lies between values of 0.4 and 0.6, while vertical dotted lines represent the speciation times for different d . In the EDM case the transition region broadens with d , whereas in the VP case it remains approximately constant in width.

B. Implementation details

Here, we provide additional implementation details to complement Section 5.1 of the main text.

Note that the expectation in Eq. 17 can be written in terms of the individual mixture components:

$$\begin{aligned}\mathbf{H}[\pi(Z)|X_t] &= -\mathbb{E} \left[\sum_{y \in \{0,1\}} \gamma_y \log \gamma_y \right] := -\mathbb{E} [h_t(x)] \\ &= - \int \left[\sum_{y \in \{0,1\}} p_t(x|Z=y) p(Z=y) \right] h_t(x) dx.\end{aligned}$$

Sampling mixture components Depending on the exact partition defined by π , the previous decomposition is necessary or useful. Necessary, when the partition is non-exhaustive, since $p_\pi(X_t)$ needs to be re-normalized (to obtain a valid entropy), and useful when it is exhaustive, i.e., $p_\pi(X_t) = p(X_t)$. The latter case would technically allow us to sample directly from the unconditional model to obtain both: samples from $p(X_t|\pi=0)$ and samples from $p(X_t|\pi=1)$. However, unconditional models are notoriously bad at generating samples with strong class-specific coherence, while they do capture the general structure of the dataset. As a consequence, samples will, with a vanishingly low probability, belong to the class of interest ($\pi=0$) and Eq. (17) will not be robust for small number of samples n .

Choosing the prior Sampling from individual components does not resolve the issue on its own, because the respective integral will be reweighted by $p(\pi=0) = |\mathcal{A}|/|Z|$, which is also vanishingly small when the set of classes is large and hence suppresses the contribution of $I_{\pi,0}^{(0)}$ (Algorithm 1). We solve this issue by choosing $p(\pi) = 0.5$ irrespective of the defined partition (the results from Section 4 still hold). Thus, the partitioned class-conditional entropy becomes equivalent to the *Jensen-Shannon Divergence* which essentially measures the overlap of individual distribution with their equally weighted mixture.

Approximating the complement When π separates the set of classes into $Z = i$ against its complement, one must sample from the complement $Z \neq i$, which, again, is infeasible in practice. As stated above, the unconditional model is good at generating the overall structure of the dataset. We therefore use $p(X_t|\pi=1) = p(X_t)$ in these cases which, moreover, becomes an increasingly better approximation as the set of classes increases.

Estimation at generation time The conditional entropy can also be computed in the forward direction. That is, the posterior can be estimated by averaging over samples drawn from the conditional training distribution $p(X_0|Z=i)$ that are then projected forward according to Eq. 6. We opted against this procedure as it does not capture the inherent errors of the model, i.e., the discrepancy between forward and learned reverse dynamics. In addition, it would require the training dataset, which in many applications is not accessible.

Entropy or entropy production Instead of Eq. (17) one can also estimate the production of the partitioned class-conditional entropy (Eq. (8)), which we derive in Appendix A.1. However, we found that estimating the posterior given the previously discussed choices offers inbuilt dynamic clamping through the ratio estimation, i.e., $p_{\text{ratio}} = p(X_t|\pi=0)/p(X_t|\pi=1)$ with $p(\pi=0|X_t) = p_{\text{ratio}}/(1+p_{\text{ratio}})$.

Estimation entropy profiles using guidance Under guidance, the entropy in Eq. (17) becomes a cross-entropy as we are replacing the expectation over the unguided mixture by the guided one. Consequently, the posterior updates are computed on the guided trajectories.

C. Experimental details & additional results

Model settings EDM2-XS Our experiments were carried out using the EDM2-XS model trained on the ImageNet-512 dataset (Deng et al., 2009). All images were generated with a stochastic DDIM sampler (Song et al., 2021a) (NFE=64) discretizing uniformly in time according to the EDM schedule with ($\sigma_{\min} = 0.002, \sigma_{\max} = 80.0, \rho = 7.0$) (Karras et al., 2022; Deng et al., 2009). The highlighted entropy profiles (no guidance, guidance) were generated using 3000 samples each, while we used 300 samples for the remainder (observed visual convergence).

Model settings SD 1.5 In the context of text-to-image we rely on Stable Diffusion 1.5 (Rombach et al., 2022) trained on LAION5B (Schuhmann et al., 2022). All images were generated using a stochastic DDIM sampler (Song et al., 2021a) (NFE=100) with a standard DDPM scheduler (Ho et al., 2020). The entropy profiles were generated using 400 samples each. However, we observed visual convergence from around 200 samples on the tested prompts.

Guidance intervals ImageNet We performed a grid search on the parameters $(\sigma_{\text{low}}, \sigma_{\text{high}}, \omega)$ using 50K samples for each setting. The metrics used for the evaluation were FID (Heusel et al., 2017), $\text{FD}_{\text{DINOv2}}$ (Stein et al., 2023), precision & recall (Kynkänniemi et al., 2019; Sajjadi et al.), and a logit classification margin based on Inception-v3. FID and $\text{FD}_{\text{DINOv2}}$ both compute the *Frechet distance* using mean and covariance estimators for real and generated image embeddings obtained from Inception-v3 (Szegedy et al., 2016) and DINOv2 (Oquab et al., 2024), respectively. Precision and recall measure the percentage of images generated that are within the data manifold and the percentage of real images that are within the generation manifold, respectively. For this purpose, we used the DINOv2 embeddings and $k = 5$ as the neighborhood size, i.e. the local manifold measure. The data manifold was approximated using 10K samples from the ImageNet-512 test set. The Inc.-v3 logit classification margin was computed by averaging the per-sample logit margins between the generated samples' classes and their nearest neighbors. That is, $\text{logit}_c(x) - \max_{i \neq c} \text{logit}_i(x)$. The optimal settings for limited interval guidance as well as full interval guidance are reported below.

$\underset{[\sigma_{\text{low}}, \sigma_{\text{high}}], \omega}{\text{argmin}} \{\cdot\}$	$[\sigma_{\text{low}}, \sigma_{\text{high}}], \omega$	FID (\downarrow)	$\text{FD}_{\text{DINOv2}} (\downarrow)$	Inc.-v3 (\uparrow)	Prec. (\uparrow)	Rec. (\uparrow)
FID	$[0.27, 1.50], 2.0$	3.55	126.8	3.85	0.889	0.752
$\text{FD}_{\text{DINOv2}}$	$[0.93, 5.28], 2.5$	7.20	87.8	4.57	0.94	0.723

Table 1. Optimal limited interval guidance settings for FID- and $\text{FD}_{\text{DINOv2}}$ along with independent evaluation metrics.

$\underset{\omega}{\text{argmin}} \{\cdot\}$	ω	FID (\downarrow)	$\text{FD}_{\text{DINOv2}} (\downarrow)$	Inc.-v3 (\uparrow)	Prec. (\uparrow)	Rec. (\uparrow)
FID	0.375	4.96	131.65	3.52	0.882	0.752
$\text{FD}_{\text{DINOv2}}$	1.25	7.42	101.15	4.59	0.927	0.686

Table 2. Optimal full guidance settings for FID- and $\text{FD}_{\text{DINOv2}}$ along with independent evaluation metrics.

C.1. Additional results ImageNet

To provide a feeling for the visual quality and diversity of the generated images under guidance, we have provided generated images for our highlighted running examples (*tiger shark, eft, paintbrush*) when using the pure conditional score, guidance in a limited interval (optimized for FID and $\text{FD}_{\text{DINOv2}}$), and guiding over the full range of noise levels (optimized for $\text{FD}_{\text{DINOv2}}$). Along with the generated images, we also show the altered entropy profiles next to the noiseless predictions over time.

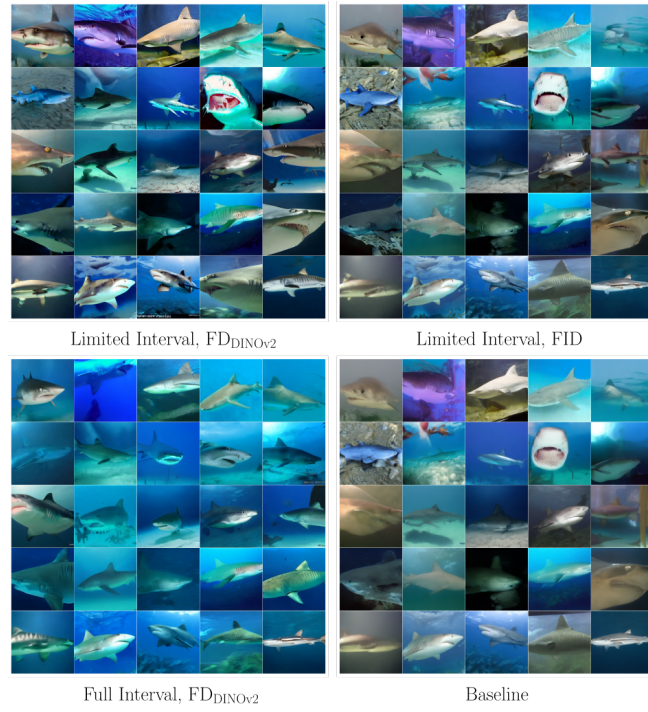


Figure 6. Generation example for the class tiger shark.

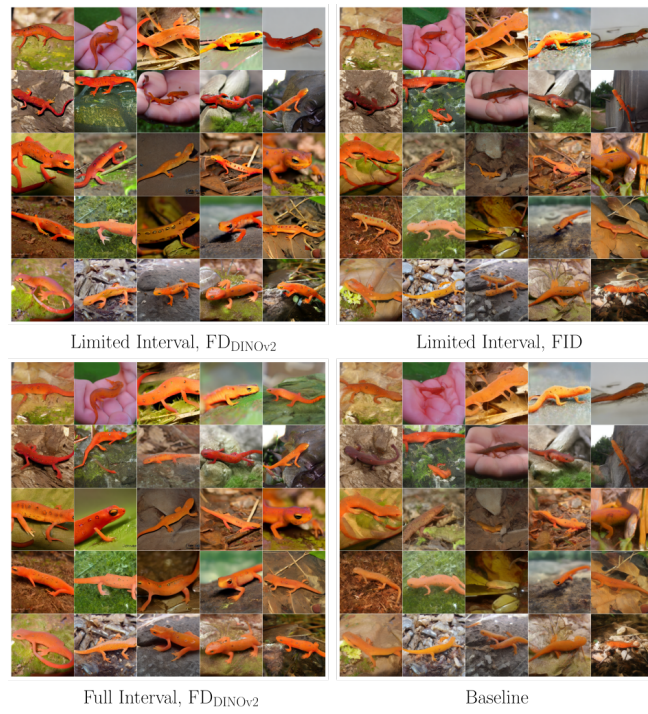


Figure 7. Generation example for the class eft.

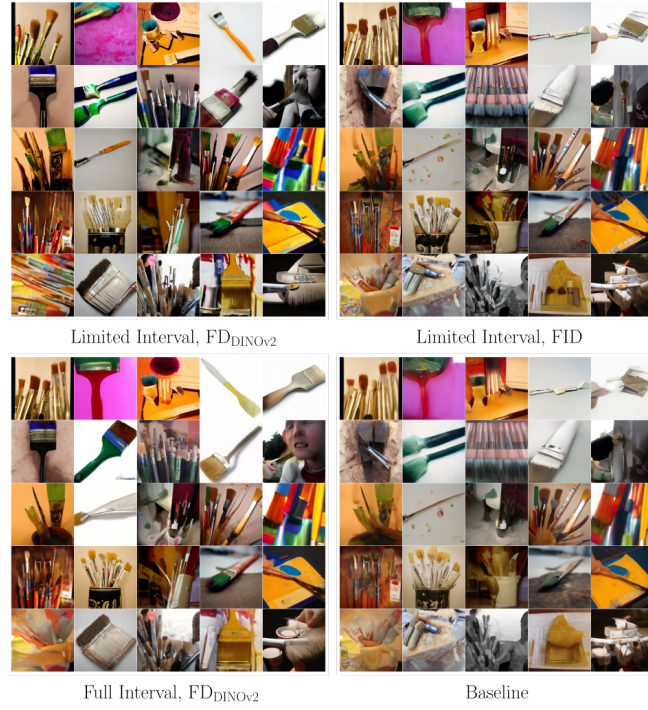


Figure 8. Generation example for the class paintbrush.

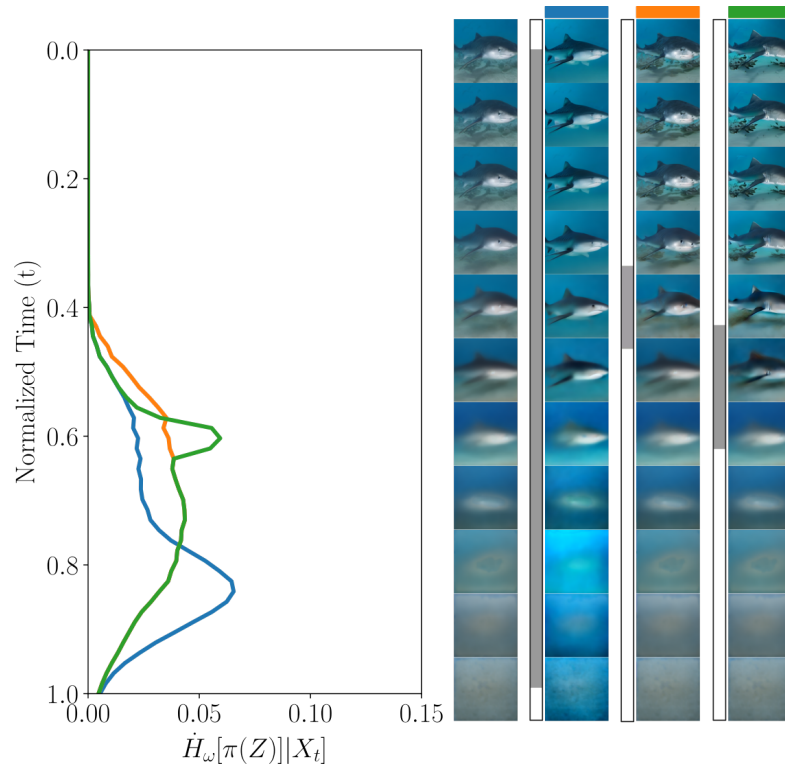


Figure 9. Distortion effects of guidance for the class tiger shark. Guidance is applied in the region colored in gray.

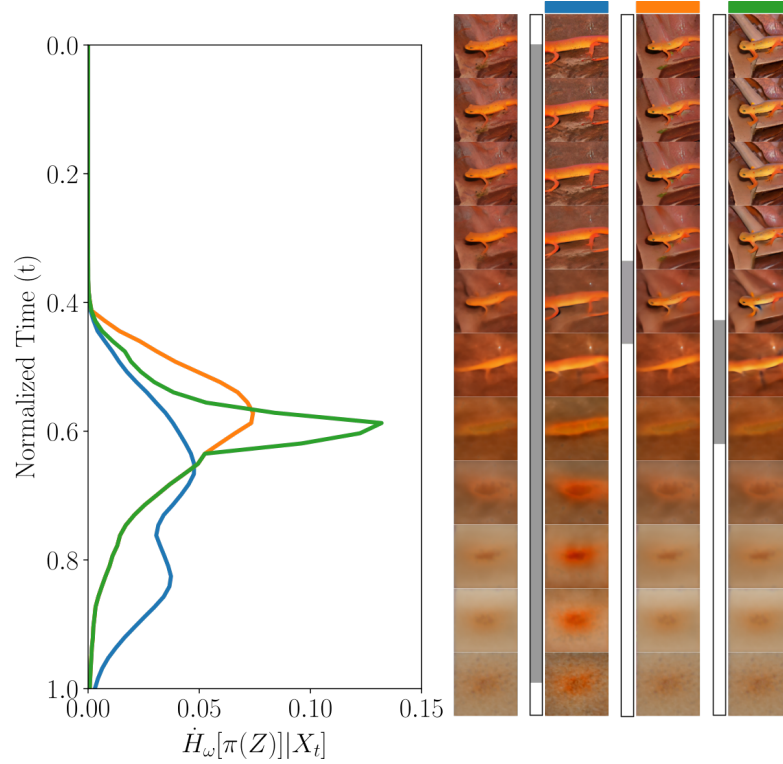


Figure 10. Distortion effects of guidance for the class eft. Guidance is applied in the region colored in gray.

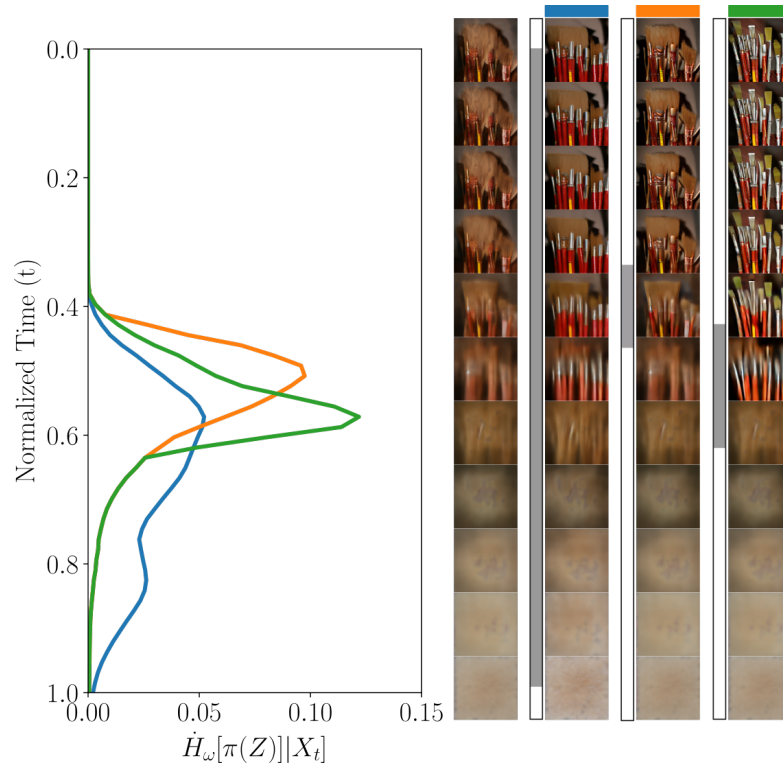


Figure 11. Distortion effects of guidance for the class paintbrush. Guidance is applied in the region colored in gray.

C.2. Additional results stable diffusion

In this section additional entropy profiles align samples, similar to the Figure 4 in the main body are provided. Two cases in which our metric fails to capture the relevant changes are also described. These are given by when the model fails to adhere to the prompt (such as the absence of the cat in the top left square in Figure 16), or when the variant prompt samples differ significantly from the base prompt samples. In the latter measuring the conditional entropy does not solely measure when the specific attribute of the variants prompt is being generated but also depends on how the variant prompt differs non-negligibly from the base prompt. Next the additional examples will be described one by one.

First two different samples using the same base and variant prompts as in the main body are shown in Figures 12 and 13. The same conclusions are visible as in the examples displayed in the main body. Again the same sequence of generation can be observed. At snapshot (a) only the low frequency prompts seem to have an impact. At snapshot (b) the windows seem to be also resolved and finally at (c) all variants of the prompt have been generated.

Secondly we show examples of entropy profiles computed on different base prompts. For this purpose we choose as base prompt *"A sports car from the front"* and *"A portrait of an orange cat"*, shown in Figures 14 and 15 respectively. We would like to emphasize that due to the poor prompt adhesion of Stable Diffusion 1.5 it can be difficult to find prompts that are modelled well enough to be used for this fine grained semantic analysis. We choose ours by verifying by hand whether the prompts were indeed followed well enough. We expect better model to simplify this pipeline drastically.

For both other chosen prompts we find similar trends, low frequency changes such as colours (e.g. *"in the snow"* or *"in black and white"*) or large objects (e.g. *"next to a building"*) are generated much earlier than smaller objects (e.g. *"wearing a hat"* or *"a cat sitting on top"*). Again a good overlap between the generated samples and the entropy curves is observed.

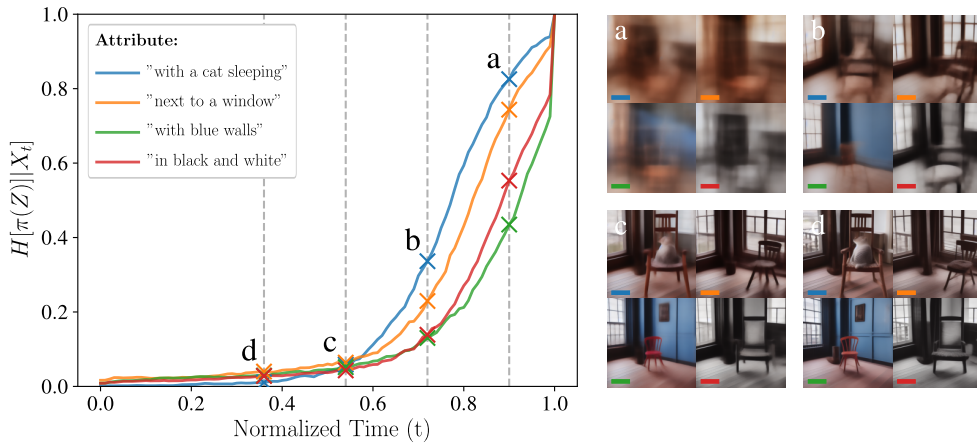


Figure 12. Entropy profiles for binary partitions of the form: “A wooden chair” vs. “A wooden chair + attribute”.

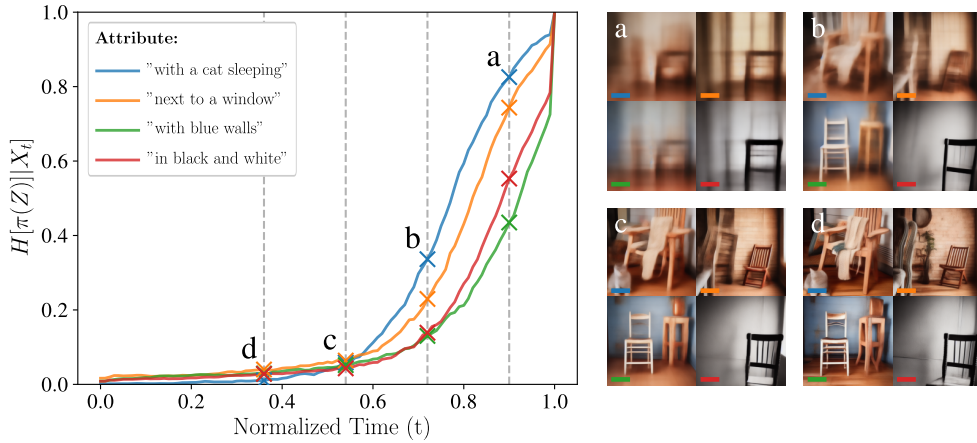


Figure 13. Entropy profiles for binary partitions of the form: “A wooden chair” vs. “A wooden chair + attribute”.

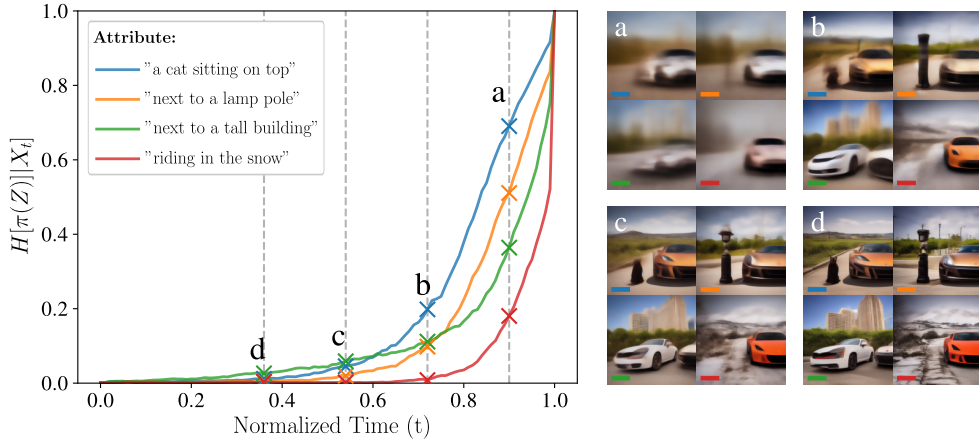


Figure 14. Entropy profiles for binary partitions of the form: “A sports car from the front” vs. “A sports car from the front + attribute”.

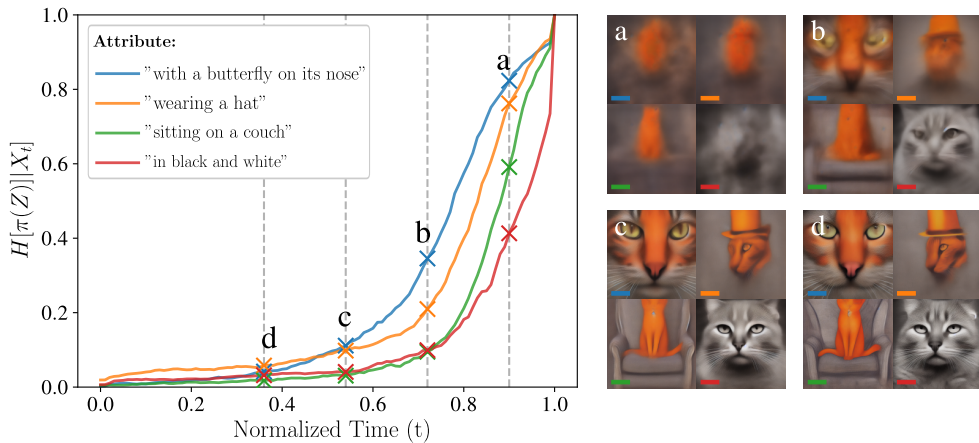


Figure 15. Entropy profiles for binary partitions of the form: “A portrait of an orange cat” vs. “A portrait of an orange cat + attribute”.

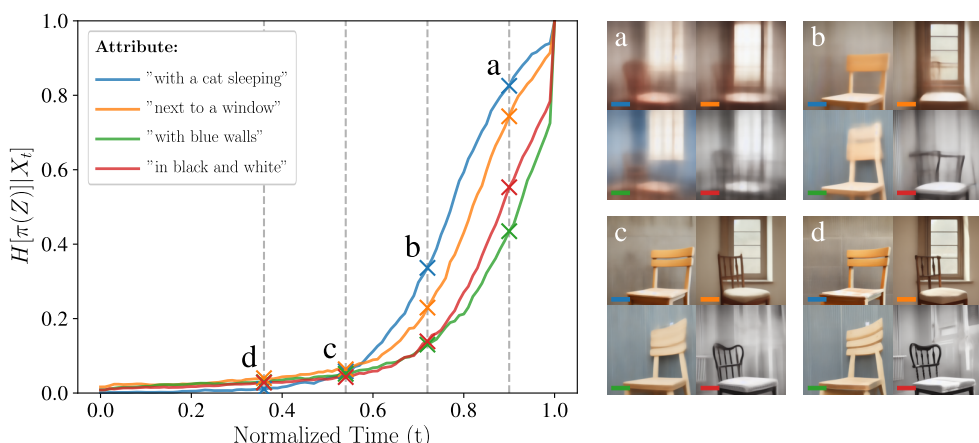


Figure 16. Illustration of a failure case: poor prompt adherence of Stable Diffusion 1.5 Entropy profiles for binary partitions of the form: “A wooden chair” vs. “A wooden chair + attribute”. In this case the failure is clearly visible in the absence of the cat in the top left sample.